University of Reading

School of Mathematical and Physical Sciences

Fast Diffusion in Porous Media

Justin Prince

August 2011

This dissertation is for a joint MSc in the Departments of Mathematics & Meteorology and is submitted in partial fulfilment of the requirements for the degree of Master of Science.

Abstract

This dissertation is concerned with the flow of chemical agents through porous media at low levels of saturation, giving rise to a fast diffusion process. A velocity based moving mesh method based upon the assumption of local mass conservation is applied to the porous medium equation in one dimensional cartesian and radial coordinates and discretised using both finite differences and finite elements. Comparisons are drawn between the fast and slow diffusive regimes, evaporation is also considered from the domain. An appropriate numerical model output in three dimensions is successfully compared to some real experimental data.

Acknowledgements

I would like to thank my supervisors, Professor Mike Baines and Doctor Alex Lukyanov for their help and advice during the course of this dissertation. I'd also like to thank the Natural Environmental Research Council for their financial support throughout this year.

Declaration

I confirm that this is my own work and the use of all material from other sources has been properly and fully acknowledged.

Signed .....

Contents

Chapter 1

Introduction

This dissertation is concerned with the application of moving meshes applied to nonlinear diffusion, specifically the porous medium equation. We shall discuss a conservation based moving mesh method based on advecting the nodes with the fluid velocity. In particular this method will be applied to modelling the dispersion of liquid chemicals in the porous medium (otherwise known as the fate of chemical agents).

1.1 Background

Exposure to chemical agents can have a major impact on the environment. Being able to model the fate of the agent accurately is therefore an extremely useful tool.

When a chemical agent is released into a porous medium, diffusion will occur and the substance will spread. The rate of diffusion depends, among other factors, on the properties of the medium as well as those of the chemical agent. To model the diffusive properties of the medium, features such as the size and coarseness of grains are considered. Also, when modelling the chemical agent, properties such as the viscosity and the temperature at which it vaporizes are important.

It is well known that a spreading liquid in a porous medium can form a capillary

bridge network, which aids the diffusive process. As described in [11], at very low levels of saturation the liquid bridges between grain particles are only connected by the thin films covering grain particles, see figure 1.1. These low levels of saturation cover a wide range of values, so understanding the change in transport properties of the medium at these levels is of vital importance. The network properties are defined by the diffusive regime imparted by these conditions.

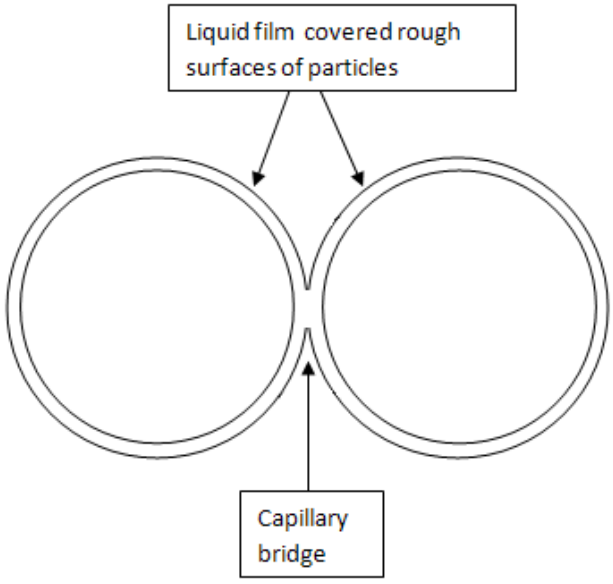

Figure 1.1: Schematic to show two grains within a porous medium at low levels of saturation

Capillary transport at low levels of liquid saturation is generally a slow process compared to diffusion at higher levels of liquid saturation [4], but it is the process responsible for the long term distribution and therefore for environmental effects.

In the situation where saturation levels are low a process can occur referred to in modelling terms as fast diffusion. The features that distinguish this fast diffusion regime from normal or slow diffusion are that the liquid is only contained in isolated capillary bridges and on the rough surface of particles.

Although modelling capillary networks around rough surfaces sounds complex, Darcy's law is used to model the transport in the porous medium. Darcy's law is formulated by considering the approximate dynamics of averaged distributions of macroscopic pressure, velocity and saturation. Information about the particular porous system and associated behaviour is contained in the functional parameters. By combining Darcy's law and mass balance the porous medium equation is derived which can be used to model liquid spreading and is described mathematically in the next chapter.

Previously, the fast diffusion process has not been measured experimentally in sufficient detail to make reliable quantitative predictions. This is due to the difficulties of understanding capillary effects on rough surfaces and in measuring liquid at low levels of saturation. However recent advances have now made this possible and we shall compare experimental results from a research group at the University of Santa Barbara [12] to those produced by the numerical model.

An important feature that has previously not been modelled in this context is the effect of evaporation on the diffusion process. Evaporation can occur by, for example, air flow over the surface of a liquid or by a supply of heat. Since we are considering the application under which we model the long term fate of a chemical agent this could be particularly important at low levels of saturation, i.e. below the threshold at which the capillary bridges break. Since this is a new feature we will concentrate on this effect from a modelling perspective.

1.2 The velocity based moving mesh approach

Throughout this dissertation we consider a velocity-based moving mesh method devised for non-linear time-dependent partial differential equations (PDE's), which has numerous physical and biological applications [3]. The method can adjust to the evolu-

tion of the solution of a PDE as well as resolving sharp features and respecting global properties. In a Lagrangian-like formulation the velocity of the mesh points is given by

$$\mathbf{v} = \frac{\partial \hat{\mathbf{x}}}{\partial t} \tag{1.1}$$

where $\mathbf{v} = \mathbf{v}(\hat{\mathbf{x}}, t)$ denotes the fluid velocity, $\hat{\mathbf{x}}(t)$ is the position of the mesh point and t is the time. By the use of time integration the mesh can be moved.

The method requires a mapping from the physical space to the velocity domain. The mesh is then modified by giving each computational node a velocity so as to advance the solution in time.

We follow earlier work on a velocity based moving mesh method which can be found in the following references [3], [6], [9], [2], [5] and [14].

Alternative adaptive mesh methods can be found in [8].

1.3 Overview of the Dissertation

The main objective of this dissertation is to take the key physical principles defined in the previous section and build a mathematical model to accurately describe them. By a quantitative comparison between some experimental results and the numerical model we hope to lay the groundwork for building a model that could be used in different research communities to give a quantitative description of capillary transport in porous media. This would allow them to predict the long-term spread of chemicals and pollutants and to deduce the environmental effects of this exposure.

In the previous section we have described the main physical concepts of the problem along with some background material. In Chapter 2 we derive the porous medium equation and relate it to the described physical problem. We also define some useful

properties of the porous medium equation.

We split Chapter 3 into two main sections for modelling diffusion by the porous medium equation which (i) excludes and (ii) includes evaporation. (i) In this first section we have the property of local mass conservation. This allows us to derive a Lagrangian velocity-based moving mesh method. This essentially takes an initial mesh and advects the nodes at the Darcy velocity using local mass conservation, allowing the solution to evolve with the mesh. (ii) In the second section we no longer have mass conservation because we include evaporation into the diffusion process. This requires us to take a slightly different approach whereby local mass fractions are conserved. Both approaches are implemented in both 1D Cartesian and d-dimensional radially symmetric coordinates. We begin modelling in 1D Cartesian coordinates since the procedure is clearer in that case. The key coordinate system for comparing the numerical model to the experimental data will be radially symmetric in 3D, allowing us to capture the hemispheric geometry of the diffusing chemical agent.

In Chapter 4, using similar principles for both mass conserving and non-mass conserving diffusion we describe a finite element formulation. We choose to include this further approach because ideally if we were to move the model into higher dimensions without radial symmetry then the finite element method would be more flexible than applying finite differences. This is because their geometrical nature can model curved boundaries more accurately.

In Chapter 5 we discuss results. Firstly we compare the fast and slow diffusive regimes to see the key differences between the two. We follow this by observing the effects of evaporation on both regimes within the numerical model. Finally we compare the most appropriate numerical model to some real experimental data, allowing us to make quantitative conclusions about the validity of the model.

We end with Chapter 6 where we conclude our findings and suggest avenues for further work in this field.

Apart from the comparison between the numerical model with some experimental data, in Chapter 5 we will not be concerned with precise physical values. Instead we shall use values that are representative of the phenomena that we expect to see.

Chapter 2

The Porous Medium Equation

The Porous Medium Equation (PME) is

$$u_t = \nabla \cdot (u^m \nabla u) \tag{2.1}$$

where $u = u(\mathbf{x}, t)$ is a non-negative scalar function in $\mathbf{x} \in \mathbb{R}^d$ and time $t \in \mathbb{R}$. The power m is the diffusion growth exponent and in most applications takes values $m \geq 1$. However for our applications we shall mostly be interested in negative values, $m < 0$, a situation known as fast diffusion.

The PME is known best for modelling an ideal gas in a homogeneous porous medium. Other applications include diffusion, heat transfer and fluid flow. Diffusion, and in particular Fast Diffusion, will be the target applications throughout this dissertation.

2.1 Derivation of the PME using Darcy's Law

We now describe the approach in [17] to derive the PME using three model equations that relate variables associated with gas flow through a porous medium.

(i) Mass balance

Also known as the continuity equation, the equation of mass conservation is given by

$$\epsilon\rho_t + \nabla \cdot (\rho \mathbf{V}) = 0 \tag{2.2}$$

where $\epsilon \in (0,1)$ is the porisity of the medium, $\mathbf{V}$ is the velocity, $\nabla\cdot$ is the divergence operator, and ρ is the density.

(ii) Darcy's Law

Darcy's Law is generally used to describe the dynamics of flows through porous media and is given by

$$\mu \mathbf{V} = -\kappa \nabla p \tag{2.3}$$

where p is the pressure of the gas, μ is the viscosity and κ is the permeability tensor which we take to be a constant.

(iii) Equation of state

An equation of state for a fluid is the ideal gas law

$$p = p_0 \rho^\gamma \tag{2.4}$$

where p_0 is some chosen reference pressure and $\gamma \geq 1$ is the specific heat ratio.

To form the PME (2.1), we first substitute (2.4) into (2.3) to give

$$\begin{aligned} \mathbf{V} &= -\frac{\kappa}{\mu} \nabla p_0 \rho^\gamma \\ &= -\frac{\kappa p_0}{\mu} \nabla \rho^\gamma \\ &= -\frac{\gamma \kappa p_0}{\mu} \rho^{\gamma-1} \nabla \rho, \end{aligned} \tag{2.5}$$

which can then be substituted into (2.2) to give

$$\rho_t = \frac{\gamma \kappa p_0}{\epsilon \mu} \nabla \cdot (\rho^\gamma \nabla \rho). \tag{2.6}$$

By writing $\rho = u$ and $\gamma = m$ and scaling out the constant $\frac{\gamma\kappa p_0}{\epsilon\mu}$ we arrive at the PME (2.1).

2.2 The PME with a source term

We also want to study the effects of evaporation by the introduction of a negative source term in (2.1), arising from mass balance. The PME with a source term is known as the CPME [17] and takes the form

$$u_t = \nabla \cdot (u^m \nabla u) + s(\mathbf{x}) \tag{2.7}$$

where $s(\mathbf{x})$ is the source term.

2.3 Initial data and boundary conditions

Due to the physical nature of the problem discussed in §1.1, we have a Dirichlet boundary condition and zero total flux at the moving boundary i.e.

$$u = u_b \text{ and } u\mathbf{v} + u^m \nabla u \cdot \hat{\mathbf{n}} = 0, \tag{2.8}$$

where $\hat{\mathbf{n}}$ is the normal to the boundary and we choose $u = u_b$ to be a small fraction of the total initial value of u. This represents the threshold value beyond which the capillary network bridges of fluid between granules of the porous media break, as described in §1.1.

In the standard PME problem $u = 0$ on the boundary, although putting $u \neq 0$ removes one of the difficulties of the equation since the standard PME is degenerate at $u = 0$. A consequence is that waiting times do not arise in this problem.

We also assume an initial data function

$$u(\mathbf{x}, 0) = u^0(\mathbf{x}) \tag{2.9}$$

2.4 Mass conservation

A property of the PME (2.1) with the boundary conditions (2.8) is conservation of mass, which we now verify using similar methods to those in [3]. For a region $\Omega(t)$ with a boundary $\partial\Omega(t)$ moving with the normal velocity $\mathbf{v}\cdot\hat{\mathbf{n}}$ we begin by differentiating the total mass integral with respect to time and applying Reynolds Transport Theorem [18], so that

$$\frac{d}{dt}\int_{\Omega(t)} u d\mathbf{x} = \int_{\Omega(t)} u_t d\mathbf{x} + \int_{\partial\Omega(t)} u\mathbf{v}\cdot\hat{\mathbf{n}} d\Gamma \tag{2.10}$$

Substituting the PME (2.1) for u_t we have

$$\frac{d}{dt}\int_{R(t)} u d\mathbf{x} = \int_{R(t)} \nabla\left(u^m \nabla u\right) d\mathbf{x} + \int_{\partial R(t)} u\mathbf{v}\cdot\hat{\mathbf{n}}\, d\Gamma \tag{2.11}$$

Using the Divergence theorem

$$\frac{d}{dt}\int_{R(t)} u d\mathbf{x} = \int_{\partial R(t)} \left(u^m \nabla u + u\mathbf{v}\right)\cdot\hat{\mathbf{n}}\, d\Gamma = 0 \tag{2.12}$$

by the zero flux boundary condition from (2.8). Since the time derivative of total mass is zero, the total mass

$$\int_{R(t)} u d\mathbf{x} = c \tag{2.13}$$

where c is a constant, therefore conserved.

A further noteworthy feature of the PME is the existence of self similar solutions. However due to the practical emphasis of this disseration we do not consider them here.

2.5 One dimensional representation of the problem

From here onwards without loss of generality the description is confined to 1D coordinate systems.

The 1D Cartesian form of (2.1) is

$$u_t = \frac{\partial}{\partial x}\left(u^m \frac{\partial u}{\partial x}\right), \tag{2.14}$$

with moving boundaries at $a(t)$ and $b(t)$, which will be solved on a moving mesh $\hat{x}_i(t)$, for $i = 0, ...N$, such that

$$a(t) = \hat{x}_0(t) < \hat{x}_1(t) < ... < \hat{x}_{N-1}(t) < \hat{x}_N(t) = b(t) \tag{2.15}$$

The boundary conditions are

$$u = u_b \text{ and } uv + u^m u_x = 0 \text{ at } \quad x(t) = a(t), b(t), \quad t > 0, \tag{2.16}$$

which are equivalent to the multi-dimensional boundary conditions (2.8).

The one dimensional version of the initial data (2.9), for (2.14) is

$$u(x, 0) = u^0(x) \tag{2.17}$$

in the region $\hat{x}_i(t^0) \in [a(t^0), b(t^0)]$. From (2.17), we choose u^0 to be symmetric in the x-axis. By the nature of the PME this symmetry will remain for all time. Therefore, from this point onwards without loss of generality we consider only the domain from 0 to any $b(t)$.

The most appropriate way to model based on the multi-dimensional physical problem in §1.1 will be as a radial 'blob' of fluid. Due to the geometrical nature of this problem we shall also look at the PME in radial coordinates

$$u_t = \frac{1}{r^{d-1}} \frac{\partial}{\partial r}\left(u^m r^{d-1} \frac{\partial u}{\partial r}\right) \tag{2.18}$$

where d is the number of dimensions. The d-dimensional radial form of the PME has the advantage that we can model a multi-dimensional process in a 1D coordinate system. However, in the radially symmetric case (2.18) adding the effects of evaporation as in (2.7) limits the model to $d = 1 \text{ or } 2$. This is because the source term acts over

the entire domain which in the case of $d = 1, 2$ is the whole domain, consistent with the physical problem. However in the case $d = 3$ modelling evaporation in this way becomes invalid as it only occurs over the boundary.

The change in boundary conditions and initial data from Cartesian to radial coordinate systems is a trivial alteration from (2.16) and (2.17) respectively.

Chapter 3

A velocity-based moving mesh method

In this chapter we describe a Lagrangian approach used to design a moving mesh method for the PME. The idea of the method is to use the principle of local mass conservation to generate a velocity with which to advance the mesh. When dealing with a mass conserving problem the velocity based moving mesh method is consistent with the total integral of the density being constant. We initially look at the mass conserving problem where there is no evaporation occuring and then at the non-mass conserving evaporation case. In both cases we go on to show how the solution u can be recovered algebraically from the new mesh and the constant masses using conservation properties.

3.1 Deriving the velocity from mass conservation

We shall describe the method to generate the velocity of the nodes from the local mass conservation principle for both the 1D Cartesian case and the radially symmetric case in d dimensions.

3.1.1 One dimension

Here we consider the PME (2.14) in one dimension, with zero flux and $u = u_b$ on the boundaries. We know that the total mass is conserved from equation (2.13) which in 1D is

$$\int_0^{b(t)} u dx = c \tag{3.1}$$

For local mass to be conserved we require it to be constant for all time. The mass from 0 to a general point $\hat{x}_i(t)$ in $(0, b(t))$ is

$$\int_0^{\hat{x}_i(t)} u dx = c_i \tag{3.2}$$

for $u > 0$. We assume that the $\hat{x}_i(t)$ are such that the c_i's are constant in time, corresponding to mass conservation in the segment from 0 to $\hat{x}_i(t)$.

We now differentiate (3.2) with respect to time and apply Leibnitz' integral rule to find that

$$\frac{d}{dt}\int_0^{\hat{x}_i(t)} u dx = \int_0^{\hat{x}_i(t)} \frac{\partial u}{\partial t} dx + \left[u\frac{dx}{dt}\right]_0^{\hat{x}_i(t)} \tag{3.3}$$

Substituting from (2.14) we have

$$\begin{aligned}
\frac{d}{dt}\int_0^{\hat{x}_i(t)} u dx &= \int_0^{\hat{x}_i(t)} \frac{\partial}{\partial x}\left(u^m \frac{\partial u}{\partial x}\right) dx + \left[u\frac{dx}{dt}\right]_0^{\hat{x}_i(t)} \\
&= \left[u^m \frac{\partial u}{\partial x} + u\frac{dx}{dt}\right]_0^{\hat{x}_i(t)} \\
&= \left[u\left(u^{m-1}\frac{\partial u}{\partial x} + \frac{dx}{dt}\right)\right]_0^{\hat{x}_i(t)} \\
&= u\left(u^{m-1}\frac{\partial u}{\partial x} + \frac{dx}{dt}\right)\Bigg|_{x=\hat{x}_i(t)} = 0
\end{aligned} \tag{3.4}$$

using the assumption that the c_i's in (3.2) are constants. We note that (3.4) is equivalent to zero total flux through all segment boundaries. We can now rearrange (3.4) to give the velocity at any point $\hat{x}_i(t)$ as

$$v_i = \frac{dx_i}{dt} = -u_i^{m-1}\left(\frac{\partial u}{\partial x}\right)_i = -\frac{1}{m}\left(\frac{\partial}{\partial x}\left(u^m\right)\right)_i \tag{3.5}$$

provided that $u_i \neq 0$. So we know that in order to preserve mass we must move nodes with this velocity. We notice at this point that the velocity (3.5) is that arising from Darcy's Law (2.3).

3.1.2 The Finite Difference Method

In the finite difference method (3.5) is approximated by

$$v_i = \frac{dx_i}{dt} = -\frac{1}{m}\left(\frac{\left(u_{i+1}^n\right)^m - \left(u_{i-1}^n\right)^m}{x_{i+1}^n - x_{i-1}^n}\right) \tag{3.6}$$

To obtain the new mesh from (3.6) we employ explicit Euler timestepping, as in

$$\frac{x_i^{n+1} - x_i^n}{\Delta t} = -\frac{1}{m}\left(\frac{\left(u_{i+1}^n\right)^m - \left(u_{i-1}^n\right)^m}{x_{i+1}^n - x_{i-1}^n}\right), \tag{3.7}$$

taking the values of x_i and u_i on the right hand side at the previous time level n. A stability condition on Δt is required, in addition to which there is a condition to prevent node overtaking also required. To do the latter we impose in effect a Lagrangian type CFL condition on the scheme, limiting the size of the timestep that we can take relative to the size of the space step such that for a general point x_i

$$|(v_{i+1} - v_i)\Delta t| < |x_{i+1} - x_i|\,, \quad \forall i, t \tag{3.8}$$

The condition (3.8) may not guarantee stability of (3.7), but by following this restriction we can prevent nodes overtaking. In practice the value of Δt is estimated by trial and error.

Conservation tells us that the c_i's in (3.2) remain constant for all time. This tells us that for a general point $\hat{x}_i(t)$ we have

$$\int_{\hat{x}_{i-1}(t^{n+1})}^{\hat{x}_{i+1}(t^{n+1})} u(x, t^{n+1})dx = \int_{\hat{x}_{i-1}(t^0)}^{\hat{x}_{i+1}(t^0)} u(x, t^0)dx \tag{3.9}$$

allowing us to find the new distribution of mass at any time. We can then use a mid-point rule to find

$$u_i(x, t^{n+1}) = \frac{c_{i+1} - c_{i-1}}{x_{i+1}(t^{n+1}) - x_{i-1}(t^{n+1})} \tag{3.10}$$

where the c_i's are from (3.2).

3.1.3 Semi-implicit timestepping

We now describe a semi-implicit timestepping method for finding the nodal position. This is useful because it allows us to take a longer timestep than with an explicit method and also prevents nodes overtaking. This method is still first order in time but avoids the Lagrangian type CFL condition (3.8), allowing larger timesteps to be taken.

We begin with a form of the scheme (3.7) for the nodal velocity formulated in §3.1.2, taking $m = 1$ for clarity. We can write

$$\begin{aligned}\frac{x_i^{n+1} - x_i^n}{\Delta t} &= -\frac{u^n_{i+\frac{1}{2}} - u^n_{i-\frac{1}{2}}}{x^n_{i+\frac{1}{2}} - x^n_{i-\frac{1}{2}}} \\ &= -\frac{u^n_{i+\frac{1}{2}}}{x^n_{i+\frac{1}{2}} - x^n_{i-\frac{1}{2}}} + \frac{u^n_{i-\frac{1}{2}}}{x^n_{i+\frac{1}{2}} - x^n_{i-\frac{1}{2}}}\end{aligned}$$

for $(1 \leq i \leq N-1)$, which can be modified without further loss of accuracy to

$$\begin{aligned}\frac{x_i^{n+1} - x_i^n}{\Delta t} &= \frac{1}{x^n_{i+\frac{1}{2}} - x^n_{i-\frac{1}{2}}}\left[-u^n_{i+\frac{1}{2}}\left(\frac{x^{n+1}_{i+1} - x^{n+1}_i}{x^n_{i+1} - x^n_i}\right) + u^n_{i-\frac{1}{2}}\left(\frac{x^{n+1}_i - x^{n+1}_{i-1}}{x^n_i - x^n_{i-1}}\right)\right] \\ &= \frac{1}{x^n_{i+\frac{1}{2}} - x^n_{i-\frac{1}{2}}}\left[\frac{u^n_{i-\frac{1}{2}}}{x^n_i - x^n_{i-1}}\left(x^{n+1}_i - x^{n+1}_{i-1}\right) - \frac{u^n_{i+\frac{1}{2}}}{x^n_{i+1} - x^n_i}\left(x^{n+1}_{i+1} - x^{n+1}_i\right)\right]\end{aligned} \tag{3.11}$$

The time accuracy is left unchanged to first order in time as can be seen from the truncation error. However this useful trick has allowed us to treat some terms implicitly. The scheme can be rearranged so that all the x_i evaluated at time $n+1$ are on the left hand side and those evaluated at n are on the right hand side, giving

$$x^{n+1}_{i-1}e^n_i + x^{n+1}_i f^n_i + x^{n+1}_{i+1}g^n_i = x^n_i \tag{3.12}$$

for $(1 \leq i \leq N-1)$, where

$$\begin{aligned} e_i^n &= -\frac{u_{i+\frac{1}{2}}\Delta t}{\left(x_i^n - x_{i-1}^n\right)\left(x_{i+\frac{1}{2}}^n - x_{i-\frac{1}{2}}^n\right)} \\ f_i^n &= 1 + \frac{u_{i-\frac{1}{2}}\Delta t}{\left(x_{i+1}^n - x_i^n\right)\left(x_{i+\frac{1}{2}}^n - x_{i-\frac{1}{2}}^n\right)} + \frac{u_{i+\frac{1}{2}}\Delta t}{\left(x_i^n - x_{i-1}^n\right)\left(x_{i+\frac{1}{2}}^n - x_{i-\frac{1}{2}}^n\right)} \\ g_i^n &= -\frac{u_{i-\frac{1}{2}}\Delta t}{\left(x_{i+1}^n - x_i^n\right)\left(x_{i+\frac{1}{2}}^n - x_{i-\frac{1}{2}}^n\right)} \end{aligned}$$

We can now determine x_i^{n+1} by inverting the tridiagonal matrix on the left hand side of the following tridiagonal system

$$\begin{pmatrix} f_1^n & g_1^n & 0 & \dots & 0 \\ e_2^n & f_2^n & g_2^n & \dots & 0 \\ \vdots & \ddots & \ddots & \ddots & \vdots \\ 0 & \dots & e_{N-2}^n & f_{N-2}^n & g_{N-2}^n \\ 0 & \dots & 0 & e_{N-1}^n & f_{N-1}^n \end{pmatrix} \begin{pmatrix} x_1^{n+1} \\ x_2^{n+1} \\ \vdots \\ x_{N-2}^{n+1} \\ x_{N-1}^{n+1} \end{pmatrix} = \begin{pmatrix} x_1^n \\ x_2^n \\ \vdots \\ x_{N-2}^n \\ x_{N-1}^n - g_{N-1}x_N^{n+1} \end{pmatrix} \tag{3.13}$$

Note that this has given us the new nodal positions, x_i^{n+1} without first calculating the velocity as in §3.1.2.

The end points x_0 and x_N are

$$x_0^{n+1} = 0 \tag{3.14}$$

$$x_N^{n+1} = x_N - \Delta t\left(\frac{u_N^n - u_{N-1}^n}{x_N^n - x_{N-1}^n}\right) \tag{3.15}$$

where x_N^{n+1} has been calculated explicitly using an upwind scheme. Because of this, we can think of (3.14) and (3.15) as Dirichlet boundary conditions for x_i^{n+1}. This is why we begin the matrix system (3.13) at x_1 and end at x_{N-1}.

From (3.11) the new distribution of x_i satisfies a maximum/minimum principle, as in [13], which prevents nodes from overtaking.

3.1.4 Radial symmetry

The radially symmetric porous medium equation (2.18) is

$$\frac{\partial u}{\partial t} = \frac{1}{r^{d-1}} \frac{\partial}{\partial r} \left(r^{d-1} u^m \frac{\partial u}{\partial r} \right) \tag{3.16}$$

where d is the number of dimensions, $r(t)$ is the radial coordinate and $u = u(r,t)$. In this section we determine the corresponding velocities for (3.16). Apart from the change in coordinate system, the boundary conditions (2.16) and initial data (2.17) remain the same. Also the total mass

$$\int_0^{b(t)} u r^{d-1} dr \tag{3.17}$$

remains constant in time

For $0 < \hat{r}_i(t) < b(t)$, the local mass conservation principle at time t is now

$$\int_0^{\hat{r}_i(t)} u r^{d-1} dr = c_i \tag{3.18}$$

and represents the total mass up to the node $\hat{r}_i(t)$.

As in §3.1.1 we shall derive velocities from the conservation of mass principle. We assume that the c_i's in (3.18) are constant in time and differentiate the integral in (3.18), applying Leibnitz' Integral rule, to give

$$\frac{d}{dt} \int_0^{\hat{r}_i(t)} u r^{d-1} dr = \int_0^{\hat{r}_i(t)} r^{d-1} \frac{\partial u}{\partial t} dr + \left[u r^{d-1} \frac{dr}{dt} \right]_0^{\hat{r}_i(t)} \tag{3.19}$$

Substituting from (3.16) we have

$$\begin{aligned}
\frac{d}{dt} \int_0^{\hat{r}_i(t)} u r^{d-1} dr &= \int_0^{\hat{r}_i(t)} r^{d-1} \left(\frac{1}{r^{d-1}} \frac{\partial}{\partial r} \left(r^{d-1} u^m \frac{\partial u}{\partial r} \right) \right) dr + \left[u r^{d-1} \frac{dr}{dt} \right]_0^{\hat{r}_i(t)} && (3.20) \\
&= \int_0^{\hat{r}_i(t)} \frac{\partial}{\partial r} \left(r^{d-1} u^m \frac{\partial u}{\partial r} \right) dr + \left[u r^{d-1} \frac{dr}{dt} \right]_0^{\hat{r}_i(t)} && (3.21) \\
&= \left[r^{d-1} u^m \frac{\partial u}{\partial r} + u r^{d-1} \frac{dr}{dt} \right]_0^{\hat{r}_i(t)} && (3.22) \\
&= r^{d-1} u \left(u^{m-1} \frac{\partial u}{\partial r} + \frac{dr}{dt} \right) \Bigg|_{\hat{r}_i(t)} = 0 && (3.23)
\end{aligned}$$

since the c_i's are constants. As before this is equivalent to zero total flux through all section boundaries.

We can rearrange (3.23) to find the velocity as in §3.1.1, giving

$$v_i = \frac{d\hat{r}_i}{dt} = -u_i^{m-1}\left(\frac{\partial u}{\partial r}\right)_i = -\frac{1}{m}\left(\frac{\partial}{\partial r}\left(u^m\right)\right)_i \tag{3.24}$$

Once again, as would expected for a mass conserving problem, we have derived the Darcy velocity as in (3.5) except in terms of the radial coordinate.

In the finite difference method using radially symmetric coordinates (3.24) is approximated as

$$v_i = \frac{dr_i}{dt} = -\frac{1}{m}\left(\frac{\left(u_{i+1}^n\right)^m - \left(u_{i-1}^n\right)^m}{r_{i+1}^n - r_{i-1}^n}\right), \tag{3.25}$$

and to find the new nodal positions $\hat{r}_i(t)$ we use explicit Euler timestepping as in §3.1.2, or semi-implicit timestepping as in §3.1.3.

Due to the conservation in each section we can use the new mesh spacing to recover the solution u, as in (3.10), which in the radial sense is

$$u_i(r, t^{n+1}) = \frac{c_{i+1} - c_{i-1}}{r_i^{d-1}(t^{n+1})\left(r_{i+1}(t^{n+1}) - r_{i-1}(t^{n+1})\right)} \tag{3.26}$$

3.2 Including evaporation from the boundary

In the remainder of the chapter we consider the evaporation case, as described physically in §1.1. In this case global mass conservation no longer applies. This requires us to take a slightly different approach to finding the nodal velocity, this time based on local conservation of mass *fractions*.

As in §3.1 we first describe the method to find the velocity in 1D Cartesian coordinates and then generalise to radially symmetric coordinates in d dimensions (although $d = 2$ is the only realistic value physically).

3.2.1 One dimension

We consider the CPME (2.7) with evaporation from the boundary in one dimension. A source term is present and for now we shall keep the general form $s(x)$ so that

$$u_t = \frac{\partial}{\partial x}\left(u^m \frac{\partial u}{\partial x}\right) + s(x) \tag{3.27}$$

where in practice $s(x)$ is negative. Evaporation will cause total the mass to reduce, eventually to zero and local mass cannot be conserved. We therefore require another way to derive the velocity. Let us define the total mass to be

$$\int_0^{b(t)} u dx = \theta(t), \tag{3.28}$$

say, which now varies with time. Taking the time derivative of (3.28) using Leibnitz Integral Rule we find that

$$\begin{aligned} \theta'(t) &= \frac{d}{dt}\int_0^{b(t)} u dx \\ &= \int_0^{b(t)} u_t dx + [uv]_0^{b(t)} \end{aligned} \tag{3.29}$$

Substituting in (3.27) we have

$$\begin{aligned} \theta'(t) &= \int_0^{b(t)} \left(\frac{\partial}{\partial x}\left(u^m \frac{\partial u}{\partial x}\right) + s(x)\right) dx + [uv]_0^{b(t)} \\ &= \left[u^m \frac{du}{dx} + uv\right]_0^{b(t)} + \int_0^{b(t)} s(x) dx \\ &= u(b)\left(u(b)^{m-1}\frac{\partial u(b)}{\partial x} + \frac{db}{dt}\right) + \int_0^{b(t)} s(x) dx \qquad (3.30) \\ &= \int_0^{b(t)} s(x) dx \qquad (3.31) \end{aligned}$$

since the first term of (3.30) vanishes by virtue of the zero total flux boundary condition in (2.16).

Although local mass cannot be conserved, the integral of u in the segment from 0 to

$\hat{x}_i(t)$ can be assumed to be a constant fraction of $\theta(t)$, so the following mass fractions integral μ_i:

$$\frac{1}{\theta(t)}\int_0^{\hat{x}_i(t)} u dx = \mu_i \tag{3.32}$$

is constant for all time. Note that $\mu_N = 1$.

We approach conservation of μ_i in a similar fashion as for the c_i in §3.1.1. We begin by multiplying both sides of (3.32) by $\theta(t)$ and taking the time derivative of the resulting equation so that

$$\begin{aligned}\frac{d}{dt}\int_0^{\hat{x}_i(t)} u dx &= \frac{d}{dt}\left(\theta(t)\mu_i\right) \\ &= \theta'(t)\mu_i \end{aligned} \tag{3.33}$$

Evaluating the left hand side of (3.33), it can be shown in a similar manner as for (3.30) that

$$\frac{d}{dt}\int_0^{\hat{x}_i(t)} u dx = u(\hat{x})\left(u(\hat{x})^{m-1}\frac{\partial u(\hat{x})}{\partial x} + \frac{d\hat{x}}{dt}\right) + \int_0^{\hat{x}_i(t)} s(x)dx$$

Now substituting (3.31), (3.32) and (3.34) into (3.33) we can rearrange to find the nodal velocity

$$\frac{d\hat{x}}{dt} = \frac{\int_0^{b(t)} s(x)dx\mu(\hat{x})}{u(\hat{x})} - u(\hat{x})^{m-1}\frac{\partial u(\hat{x})}{\partial x} - \frac{1}{u(\hat{x})}\int_0^{\hat{x}_i(t)} s(x)dx \tag{3.34}$$

which consists of the Darcy velocity (3.5), together with a contribution from the source term. As in §3.1, we can employ explicit Euler timestepping for $\hat{x}_i(t)$ or use semi-implicit timestepping, although the latter requires the terms in (3.34) to be written as a derivative.

Conservation of partial mass in each segment tells us that the μ_i's in (3.32) remain constant in time, therefore for a general point $\hat{x}_i(t)$

$$\mu_i = \frac{\int_{\hat{x}_{i-1}(t^{n+1})}^{\hat{x}_{i+1}(t^{n+1})} u(x,t^{n+1})dx}{\int_0^{b(t^{n+1})} u(x,t^{n+1})dx} = \frac{\int_{\hat{x}_{i-1}(t^0)}^{\hat{x}_{i+1}(t^0)} u(x,t^0)dx}{\int_0^{b(t^0)} u(x,t^0)dx} \tag{3.35}$$

allowing us to find the solution u at any time. As with the conservation form we use a mid-point rule to find the new distribution of u such that

$$u_i(x, t^{n+1}) = \theta(t^{n+1}) \frac{\mu_{i+1}(x) - \mu_{i-1}(x)}{x_{i+1}(t^{n+1}) - x_{i-1}(t^{n+1})} \tag{3.36}$$

where $\theta(t^{n+1}) = \theta(t^n) + \Delta t \theta'(t^{n+1})$ and $\theta'(t^{n+1})$ can be found directly after each redistribution of nodes using a discretisation of (3.31).

3.2.2 Radial symmetry

We now find the velocity of the nodes in the radial case when evaporation is occurring from the boundary. The radially symmetric PME with a source term is

$$\frac{\partial u}{\partial t} = \frac{1}{r^{d-1}} \frac{\partial}{\partial r} \left(r^{d-1} u^m \frac{\partial u}{\partial r} \right) + s(r) \tag{3.37}$$

where in practice $s(r)$ is negative. In the application described in §1.1 we may physically only take $d = 1, 2$ as explained in §2.5.

Due to the mass reduction caused by evaporation we shall, as in §3.2.1, define the partial mass as a fraction of the total mass, which is assumed to be conserved. We define the total mass as

$$\int_0^{b(t)} u r^{d-1} dr = \theta(t), \tag{3.38}$$

say, which varies with time. Taking the time derivative of (3.38) we find that

$$\begin{aligned} \theta'(t) &= \frac{d}{dt} \int_0^{b(t)} u r^{d-1} dr \\ &= \int_0^{b(t)} r^{d-1} u_t dr + [u r^{d-1} v]_0^{b(t)} \end{aligned}$$

Substituting in (3.37) we have

$$\begin{aligned}
\theta'(t) &= \int_0^{b(t)} r^{d-1}\left(\frac{1}{r^{d-1}}\frac{\partial}{\partial r}\left(r^{d-1}u^m\frac{\partial u}{\partial r}\right)\right) + r^{d-1}s(r)dr + [ur^{d-1}v]_0^{b(t)} \\
&= \left[r^{d-1}u^m\frac{\partial u}{\partial r} + ur^{d-1}v\right]_0^{b(t)} + \int_0^{b(t)} s(r)dr \\
&= u(b)r(b)^{d-1}\left(u(b)^{m-1}\frac{\partial u(b)}{\partial r} + \frac{db}{dt}\right) + \int_0^{b(t)} s(r)r^{d-1}dr \qquad (3.39) \\
&= \int_0^{b(t)} s(r)r^{d-1}dr \qquad (3.40)
\end{aligned}$$

where the first term of (3.39) vanishes by the zero flux boundary condition in (2.16).

The integral of u from 0 to $\hat{r}_i(t)$ is now assumed to be a constant fraction of $\theta(t)$ so the following mass fraction integral μ_i:

$$\frac{1}{\theta(t)}\int_0^{\hat{r}_i(t)} ur^{d-1}dr = \mu_i \qquad (3.41)$$

is constant for all time.

We approach the conservation of μ_i as we did in §3.2.1, except for the radial case. We begin by multiplying both sides of (3.41) by $\theta(t)$ and then taking the time derivative of the resulting equation so that

$$\begin{aligned}
\frac{d}{dt}\int_0^{\hat{r}_i(t)} udr &= \frac{d}{dt}\left(\theta(t)\mu_i\right) \qquad (3.42) \\
&= \theta'(t)\mu_i \qquad (3.43)
\end{aligned}$$

Evaluating the left hand side of this, for a general point $\hat{r}_i(t)$ it can be shown in a similar manner as for (3.39) that

$$\frac{d}{dt}\int_0^{\hat{r}_i(t)} ur^{d-1}dr = u(\hat{r}_i)\hat{r}_i\left(u(\hat{r}_i)^{m-1}\frac{\partial u(\hat{r}_i)}{\partial r} + \frac{d\hat{r}_i}{dt}\right) + \int_0^{\hat{r}_i(t)} s(r)r^{d-1}dr \qquad (3.44)$$

Now substituting (3.40), (3.41) and (3.44) into (3.42) we can rearrange to find the nodal velocity

$$\frac{d\hat{r}_i}{dt} = \frac{\int_0^{b(t)} s(r)r^{d-1}dr\mu(\hat{r}_i)}{\hat{r}_i^{d-1}u(\hat{r}_i)} - u(\hat{r}_i)^{m-1}\frac{\partial u(\hat{r}_i)}{\partial r} - \frac{1}{\hat{r}_i u(\hat{r}_i)}\int_0^{\hat{r}_i(t)^{d-1}} s(r)r^{d-1}dr \qquad (3.45)$$

which as in §3.2.1 consisits of the Darcy velocity together with other terms due to the source. We can therefore employ the same timestepping methods as for (3.34) to recover the new mesh spacing.

Due to the conservation of partial mass in each section we can use the new mesh spacing to recover the solution u. We apply a mid-point rule to (3.41) to give

$$u_i(r, t^{n+1}) = \theta(t^{n+1}) \frac{\mu_{i+1}(x) - \mu_{i-1}(x)}{r_i^{d-1}(t^{n+1}) \left(r_{i+1}(t^{n+1}) - r_{i-1}(t^{n+1})\right)} \tag{3.46}$$

where $\theta(t^{n+1}) = \theta(t^n) + \Delta t \theta'(t^{n+1})$ and $\theta'(t^{n+1})$ can be found directly after each redistribution of nodes using (3.40).

3.3 The Finite Difference Algorithm

Without loss of generality, we write the algorithms for Cartesian coordinates, as it is a trivial change to use radial coordinates. We shall be solving this problem on a mesh $\hat{x}_i$, for $i = 0, ...N$, such that

$$a(t) = \hat{x}_0(t) < \hat{x}_1(t) < ... < \hat{x}_{N-1}(t) < \hat{x}_N(t) = b(t) \tag{3.47}$$

with moving boundaries at $a(t)$ and $b(t)$, where the movement of $\hat{x}_i(t)$ is caused by the zero flux condition across the interior boundaries. This is done by using the following algorithms to evolve the initial data (2.17).

3.3.1 PME in Conservation form (no evaporation)

Given the mesh and the solution at an initial time t^0, the algorithm is:

1. Compute the initial total mass c_i^0 up to each node $\hat{x}_i(t)$

$$c_i^0 = \int_0^{\hat{x}_i(t^0)} u^0 dx \tag{3.48}$$

2. Compute the nodal velocity as in §3.1.1. (If using the semi-implicit method as in §3.1.3 skip to step 4.)

3. Compute the updated mesh using

$$x_i^{n+1} = x_i^n + \Delta t\, v_i \tag{3.49}$$

where Δt is the time-step.

4. Recover the new mass distribution as described in §3.1.2 using the initial masses c_i^0 found in step one of this algorithm.

5. Repeat previous three steps for chosen number of time steps

3.3.2 PME in Non-conservation form (with evaporation)

Given the mesh $\hat{x}_i(t^0)$ and solution $u(\hat{x}_i, t^0)$ at initial time t_0, the algorithm is:

1. Compute the initial total mass $\theta(t^0)$

$$\theta(t^0) = \int_0^{b(t^0)} u^0 dx \tag{3.50}$$

and also the initial partial masses

$$c_i^0 = \int_0^{\hat{x}_i(t^0)} u^0 dx \tag{3.51}$$

and then compute the mass fractions μ_i

$$\mu_i = \frac{\int_0^{\hat{x}_i(t^0)} u^0 dx}{\int_0^{\hat{b}(t^0)} u^0 dx} \tag{3.52}$$

2. Compute the nodal velocity as in (3.34).

3. Compute the updated mesh using

$$x_i^{n+1} = x_i^n + \Delta t\, v_i. \tag{3.53}$$

and the new total mass

$$\theta^{n+1} = \theta^n + \Delta t\ (\theta')^n \tag{3.54}$$

4. With the new partial mass

$$c_i = \mu_i \theta^{n+1} \tag{3.55}$$

recover the new mass distribution, using (3.36), with the partial mass fractions μ_i's found in step one of this algorithm.

5. Repeat previous four steps for chosen number of timesteps

Chapter 4

Finite element formulation

In this chapter we describe a finite element approach to deriving a moving mesh method for the PME. As in the previous chapter we describe the method based on the assumption of local mass conservation (consistent with the total integral of density being constant). The method will firstly be used to find the velocity of nodes in the non-evaporation case where conservation applies, and then in the evaporation case where conservation no longer applies.

The finite element formulation combines a particular finite representation of the solution u with a weak form of the PME. To implement this we introduce a weak form of the conservation principle using a continuous and once-differentiable test function w_i for $(0 \leq i \leq N)$ advected with the mesh velocity v. We define a distributed mass c_i as

$$\int_0^{b(t)} w_i u dx = c_i \tag{4.1}$$

for $(0 \leq i \leq N)$.

So as not to alter the total mass of the problem we require the w_i's to be a partition of unity, so that

$$\sum_{j=0}^{N} w_j = 1 \tag{4.2}$$

Here we choose w to be a standard piecewise linear finite element hat function ϕ_i where

$$\phi_i = \begin{cases} \frac{x_{i+1}-x}{x_{i+1}-x_i} & \text{if } x \in (x_i, x_{i+1}); \\ \frac{x-x_{i-1}}{x_i-x_{i-1}} & \text{if } x \in (x_{i-1}, x_i); \\ 0 & \text{otherwise.} \end{cases} \tag{4.3}$$

for $(2 \leq i \leq N-1)$ (with suitable modifications at $i = 0, N$), which agrees with the condition (4.2) enforced upon w whilst at the same time providing useful compact support. The solution u is a linear combination of the basis functions (4.3).

4.1 Deriving the velocity from mass conservation

4.1.1 1D finite element method

We now propose a mass conservation principle in which the distributed mass c_i will remain constant for all time. As in §3.1.1, to get the velocity we differentiate the mass and apply Leibnitz' Integral rule to (4.1) so that

$$\begin{aligned} \frac{d}{dt}\left(\int_0^{b(t)} \phi_i u dx\right) &= \int_0^{b(t)} \frac{\partial(\phi_i u)}{\partial t} dx + [\phi_i uv]_0^{b(t)} \\ &= \int_0^{b(t)} \left(\frac{\partial(\phi_i u)}{\partial t} + \frac{\partial}{\partial x}(\phi_i uv)\right) dx \\ &= \int_0^{b(t)} \left(\phi_i \frac{\partial u}{\partial t} + u\frac{\partial \phi_i}{\partial t} + \phi_i \frac{\partial(uv)}{\partial x} + (uv)\frac{\partial \phi_i}{\partial x}\right) dx \\ &= \int_0^{b(t)} \left(\phi_i \left(\frac{\partial u}{\partial t} + \frac{\partial(uv)}{\partial x}\right) + u\left(\frac{\partial \phi_i}{\partial t} + v\frac{\partial \phi_i}{\partial x}\right)\right) dx \\ &= \int_0^{b(t)} \phi_i \left(\frac{\partial u}{\partial t} + \frac{\partial(uv)}{\partial x}\right) dx \qquad (4.4) \\ &= 0 \qquad (4.5) \end{aligned}$$

for $(0 \leq i \leq N)$ since the c_i's in (4.1) are assumed constant and the ϕ_i's are advected with speed v, so that $\frac{\partial \phi_i}{\partial t} + v\frac{\partial(\phi_i)}{\partial x} = 0$. Now substituting a weak form of the one-

dimensional Cartesian PME (2.14),

$$\frac{d}{dt}\left(\int_0^{b(t)} \phi_i u dx\right) = \int_0^{b(t)} \phi_i \left(\frac{\partial}{\partial x}\left(u^m \frac{\partial u}{\partial x}\right) + \frac{\partial (uv)}{\partial x}\right) dx = 0 \tag{4.6}$$

Integrating (4.6) by parts we find

$$\begin{aligned}
\int_0^{b(t)} \phi_i \left(\frac{\partial}{\partial x}\left(u^m \frac{\partial u}{\partial x}\right) + \frac{\partial (uv)}{\partial x}\right) dx &= \left[\phi_i \left(u^m \frac{\partial u}{\partial x} + uv\right)\right]_0^{b(t)} \\
&\quad - \int_0^{b(t)} \frac{\partial \phi_i}{\partial x}\left(u^m \frac{\partial u}{\partial x} + (uv)\right) dx \quad (4.7) \\
&= - \int_0^{b(t)} \frac{\partial \phi_i}{\partial x}\left(u^m \frac{\partial u}{\partial x} + (uv)\right) dx \quad (4.8) \\
&= 0, \quad (4.9)
\end{aligned}$$

for $(0 \leq i \leq N)$. The first term of (4.7) is zero since there is zero flux flowing through the boundary $b(t)$. As we seek the velocity, equation (4.8) is rearranged to give

$$\int_0^{b(t)} \frac{\partial \phi_i}{\partial x} uv dx = - \int_0^{b(t)} \frac{\partial \phi_i}{\partial x} u^m \frac{\partial u}{\partial x} dx \tag{4.10}$$

for $(0 \leq i \leq N)$. Since

$$\begin{aligned}
\sum_{i=0}^{N} \phi_i &= 1 \quad (4.11) \\
\Rightarrow \sum_{i=0}^{N} \frac{\partial \phi_i}{\partial x} &= 0 \quad (4.12)
\end{aligned}$$

the left hand side of (4.10) gives only $N-1$ independant equations. To get around this problem we impose one value of v as a Dirichlet condition.

An alternative approach is to rewrite v in terms of a velocity potential ψ where

$$v = \frac{\partial \psi}{\partial x} \tag{4.13}$$

Expanding $\frac{\partial \psi}{\partial x}$ in a series of ϕ_i's we have

$$\frac{\partial \psi}{\partial x} = \sum_{j=0}^{N} \psi_j \frac{\partial \phi_j}{\partial x} \tag{4.14}$$

We subsitute (4.14) into the left hand side of (4.10) to give

$$\int_0^{b(t)} \frac{\partial \phi_i}{\partial x} u \psi dx = \int_0^{b(t)} \frac{\partial \phi_i}{\partial x} u \sum_{j=0}^{N} \psi_j \frac{\partial \phi_j}{\partial x} dx \tag{4.15}$$

$$= \sum_{j=0}^{N} \int_0^{b(t)} u \frac{\partial \phi_i}{\partial x} \frac{\partial \phi_j}{\partial x} dx \psi_j \tag{4.16}$$

for $(0 \leq i \leq N)$. Again since the ϕ's constitute a partition of unity there are only $N-1$ independent equations, but without loss of generality we can set $\psi = 0$ at an arbitrary point.

Substituting (4.16) into (4.10) leads to the matrix system

$$K\underline{\psi} = \underline{f} \tag{4.17}$$

where K is a singular matrix, known as the stiffness matrix. In this case the K matrix is the following tridiagonal system

$$K = \begin{pmatrix} K_{0,0} & K_{0,1} & 0 & \dots & 0 \\ K_{1,0} & K_{1,1} & K_{1,2} & \dots & 0 \\ \vdots & \ddots & \ddots & \ddots & \vdots \\ 0 & \dots & K_{N-1,N-2} & K_{N-1,N-1} & K_{N-1,N} \\ 0 & \dots & 0 & K_{N,N-1} & K_{N,N} \end{pmatrix}$$

where

$$\begin{aligned} K_{0,0} &= \frac{u_1 + u_2}{2(x_2 - x_1)} \\ K_{i,i} &= \frac{u_i + u_{i-1}}{2(x_i - x_{i-1})} + \frac{u_i + u_{i+1}}{2(x_i - x_{i+1})} \\ K_{i,i+1} &= \frac{u_i + u_{i+1}}{2(x_i - x_{i+1})} \\ K_{i+1,i} &= \frac{u_i + u_{i-1}}{2(x_i - x_{i-1})} \\ K_{N,N} &= \frac{u_N + u_{N-1}}{2(x_N - x_{N-1})} \end{aligned}$$

As we can see from the K matrix entries, we have averaged u across the nodes. This is because it is a linear function of x.

Imposing $\psi = 0$ at any point and reducing the system (4.17) accordingly we get

$$K_r \underline{\psi}_r = \underline{f}_r \tag{4.18}$$

where K_r, $\underline{\psi}_r$ and $\underline{f}_r$ are K, $\underline{\psi}$ and $\underline{f}$ modified by $\psi = 0$ at one point. Then K_r is non-singular and

$$\Rightarrow \underline{\psi}_r = K_r^{-1} \underline{f}_r \tag{4.19}$$

Once we have recovered ψ, we can differentiate to find the velocity. However, due to the way in which we have calculated ψ the derivative will only give us accurate values of v halfway between nodes. The following equation then linearly interpolates v to the nodes:

$$v_{node\,i} = \frac{\frac{v_{i-\frac{1}{2}}}{x_i - x_{i-1}} + \frac{v_{i+\frac{1}{2}}}{x_{i+1} - x_i}}{\frac{1}{x_i - x_{i-1}} + \frac{1}{x_{i+1} - x_i}}, \tag{4.20}$$

which is known to be exact for linear v, see [15]. We now have the velocities, allowing us to find the new positions of nodes x_i using explicit Euler timestepping.

4.1.2 Recovering the solution u

Unlike in the finite difference case, it is non-trivial to calculate new values for $u(x)$ at the end of each iteration and we have to solve another matrix system. Beginning with the weak mass conservation principle (4.1) with w_i replaced by ϕ_i, we expand $u(x)$ in terms of the basis function ϕ so that

$$u(x) = \sum_{j=0}^{N} u_j \phi_j(x) \tag{4.21}$$

Substituting this in to (4.1) we find

$$\begin{aligned} \int_0^{b(t)} \phi_i(x) u(x) dx &= \int_0^{b(t)} \phi_i(x) \sum_{j=0}^{N} u_j \phi_j(x) dx \\ &= \sum_{j=0}^{N} \int_0^{b(t)} \phi_i(x) \phi_j(x) dx u_j = c_i \end{aligned} \tag{4.22}$$

which results in the matrix system

$$M\underline{u} = \underline{c} \tag{4.23}$$

where M is a non-singular mass matrix and $\underline{c}$ is a vector of c_i's which can be pre-computed at $t = t_0$, that we can solve for (4.22). Hence

$$\underline{u} = M^{-1}\underline{c} \tag{4.24}$$

The coefficient matrix M is tridiagonal of the form

$$M = \begin{pmatrix} M_{0,0} & M_{0,1} & 0 & \dots & \dots & \dots & 0 \\ M_{1,0} & M_{1,1} & M_{1,2} & 0 & & & \vdots \\ 0 & \ddots & \ddots & \ddots & & & \vdots \\ \vdots & & M_{i,i-1} & M_{i,i} & M_{i,i+1} & & \vdots \\ \vdots & & & \ddots & \ddots & \ddots & 0 \\ \vdots & & & & M_{N-1,N-2} & M_{N-1,N-1} & M_{N-1,N} \\ 0 & \dots & \dots & \dots & 0 & M_{N,N-1} & M_{N,N} \end{pmatrix}$$

with entries

$$\begin{aligned} M_{0,0} &= \frac{x_1 - x_0}{3} \\ M_{i,i} &= \frac{x_{i+1} - x_i}{6} + \frac{x_i - x_{i-1}}{6} \\ M_{i,i+1} &= \frac{x_{i+1} - x_i}{6} \\ M_{i+1,i} &= \frac{x_i - x_{i-1}}{6} \\ M_{N,N} &= \frac{x_N - x_{N-1}}{3} \end{aligned}$$

4.2 Deriving the velocity with evaporation

4.2.1 1D finite element method

For the non mass-conserving finite element method with evaporation we once again assume conservation of partial mass fractions to deduce the velocity as in §3.2. We

begin with the total mass

$$\int_0^{b(t)} u dx = \theta(t), \tag{4.25}$$

which varies with time. The derivative of (4.25) has already been shown in §3.2.1 to be

$$\theta' = \int_0^{b(t)} s(x) dx \tag{4.26}$$

We also define the distributed mass from 0 to $b(t)$ as

$$\int_0^{b(t)} \phi_i u dx \tag{4.27}$$

We express the distributed mass as a fraction of the total mass to give

$$\frac{1}{\theta(t)} \int_0^{b(t)} \phi_i u dx = \nu_i \tag{4.28}$$

which we assume to be constant in time. Now multiplying both sides of (4.28) by $\theta(t)$ and taking the time derivative we have

$$\frac{d}{dt} \int_0^{b(t)} \phi_i u dx = \nu_i \theta'(t) \tag{4.29}$$

We now evaluate the left hand side of (4.29). From (4.4) we have

$$\frac{d}{dt} \int_0^{b(t)} \phi_i u dx = \int_0^{b(t)} \phi_i \left(\frac{\partial u}{\partial t} + \frac{\partial (uv)}{\partial x} \right) dx \tag{4.30}$$

Substituting equation (3.27) into (4.30) gives us

$$= \int_0^{b(t)} \phi_i \left(\frac{\partial}{\partial x} \left(u^m \frac{\partial u}{\partial x} \right) + s(x) + \frac{\partial (uv)}{\partial x} \right) dx \tag{4.31}$$

Integrating (4.31) by parts, we have

$$\begin{aligned} \frac{d}{dt} \int_0^{b(t)} \phi_i u dx &= \left[\phi_i \left(u^m \frac{\partial u}{\partial x} + \int_0^{b(t)} s(x) dx + uv \right) \right]_0^{b(t)} \\ &\quad - \int_0^{b(t)} \frac{\partial \phi_i}{\partial x} \left(u^m \frac{\partial u}{\partial x} + \int_0^{b(t)} s(x) dx + uv \right) dx \qquad (4.32) \\ &= \left[\phi_i \int_0^{b(t)} s(x) dx \right]_0^{b(t)} \\ &\quad - \int_0^{b(t)} \frac{\partial \phi_i}{\partial x} \left(u^m \frac{\partial u}{\partial x} + \int_0^{b(t)} s(x) dx + uv \right) dx \qquad (4.33) \end{aligned}$$

where we have used the zero flux boundary condition from (2.16).

Putting this all together into (4.29), we rearrange to make the velocity term the subject giving

$$\begin{aligned}\int_0^{b(t)} \frac{\partial \phi_i}{\partial x} uv dx &= \left[\phi_i \int_0^{b(t)} s(x)dx\right]_0^{b(t)} \\ &\quad - \int_0^{b(t)} \frac{\partial \phi_i}{\partial x}\left(u^m \frac{\partial u}{\partial x}\int_0^{b(t)} s(x)dx\right)dx \\ &\quad + \mu_i \int_0^{b(t)} s(x)dx \end{aligned} \tag{4.34}$$

We can treat this in an almost identical way, as we did (4.10), the only difference being the right hand side which we now call $\underline{f}$. Once again we write the velocity as the derivative of the velocity potential and solve the matrix system

$$K\underline{\psi} = \underline{f} \tag{4.35}$$

from which we find the velocity potentials ψ. As in §4.1.1 we can differentiate ψ to find the velocity and then interpolate, using equation (4.20), to recover v at the nodes.

4.2.2 Recovering the solution u with evaporation

As in §4.1.2 the solution u can be recovered directly from the finite element form. Since the ν_i's are constant for all time we have

$$\nu_i = \frac{1}{\theta(t)}\int_0^{b(t)} \phi_i(x)u(x)dx = \left[\frac{1}{\theta(t)}\int_0^{b(t)} \phi_i(x)u(x)dx\right]_{t=t_0} \tag{4.36}$$

As in §4.1.2 we expand $u(x)$ in terms of the basis function ϕ and the partial mass at time t from (4.36) becomes

$$\frac{1}{\theta(t)}\int_0^{b(t)} \phi_i u dx = \int_0^{b(t)} \phi_i(x)\sum_{j=0}^{N} u_j\phi_j(x)dx \tag{4.37}$$

$$= \sum_{j=0}^{N}\int_0^{b(t)} \phi_i(x)\phi_j(x)dx u_j = \nu_i \tag{4.38}$$

This results in the non-singular matrix system

$$M\underline{u} = \underline{d} \tag{4.39}$$

$$\Rightarrow \underline{u} = M^{-1}\underline{d} \tag{4.40}$$

The only difference between this matrix system and (4.24) is the right hand side. The vector $\underline{d}$ in this instance is

$$\underline{d} = \theta(t)\underline{\nu} \tag{4.41}$$

found by rearranging (4.36).

Using the M matrix as defined in §4.1.2 we now have all of the information required to recover the solution u.

4.3 1D Finite Element algorithm

For the 1D finite element algorithm we begin with the initial mesh, with nodes, $x_i(t^0)$ for $i = 0, 1, ...N$, with boundary conditions (2.16) and initial data (2.17).

4.3.1 Mass conserving algorithm

Given the mesh and solution at initial time t^0, the algorithm is:

1. Compute the constant distributed masses c_i of the segments using the mass integral (4.1) at time t^0

2. Compute the nodal velocity by following the method using the velocity potential described in §4.1

3. Compute the updated mesh using

$$x_i^{n+1} = x_i^n + \Delta t\, v_i \tag{4.42}$$

4. Compute the new solution by solving the matrix system (4.24) where the right hand side can be computed using the c_i's from step 1.

5. Repeat the previous four steps for the chosen number of time steps.

4.3.2 Non mass-conserving algorithm (with evaporation)

Given the mesh and solution at initial time t^0, the algorithm is:

1. Compute the initial total mass $\theta(t^0)$

$$\int_0^{b(t^0)} u^0 dx = \theta(t^0) \tag{4.43}$$

the weak form of the initial masses d_i

$$\int_0^{\hat{x}_i(t^0)} \phi_i u^0 dx = d_i. \tag{4.44}$$

and the mass fractions μ_i

$$\nu_i = \frac{\int_0^{b(t^0)} \phi_i u^0 dx}{\int_0^{b(t^0)} u^0 dx} \tag{4.45}$$

2. Compute the nodal velocitys from the velocity potentials as described in §4.2.1.

3. Compute the updated mesh using

$$x_i^{n+1} = x_i^n + \Delta t\, v_i. \tag{4.46}$$

Use the new mesh distribution to calculate $\theta'(t^{n+1})$ directly from (4.26) and from this the new total mass

$$\theta(t^{n+1}) = \theta(t^n) + \Delta t\, \theta'(t^{n+1}) \tag{4.47}$$

4. Use the new total mass (4.47) to recover the solution u as described in §4.2.2.

5. Repeat the previous four steps for the chosen number of time steps.

Chapter 5

Results

We split the results chapter into two main sections. We begin by presenting numerical results for the methods described in Chapter 3 and Chapter 4, followed by a comparison of the numerical model with some real data.

5.1 Numerical results

We first describe numerical results for the methods derived in Chapter 3 and Chapter 4. We pay particular attention to the differences between fast diffusion and slow diffusion and also the effects of evaporation. Since the various methods described provide similar results we do not show them all for each one. Instead we display results for chosen cases, illustrating the various methods described.

We begin by comparing results for fast diffusion and slow diffusion using the mass conserving 1D finite element model derived in §4.1. We analyse several plots that have been produced to give good supporting arguments to our observations, allowing us to deduce the various behaviour.

We then investigate the effects of evaporation on the two dimensional radially symmetric PME for both the fast and slow diffusive regimes. We show that we can force

retreat of the boundary in both cases.

5.1.1 The Numerical model test problem

To run the numerical model we need to define boundary conditions and initial data. This is chosen specifically to demonstrate behaviour representative of the physical phenomena described in §1.1. The boundary conditions (2.16) are defined as

$$u = 0.1 \text{ and } uv + u^m u_x = 0 \text{ at } \quad x(t) = a(t), b(t), \quad t > 0, \tag{5.1}$$

where $u = 0.1$ is representative of the threshold value beyond which the capillary network bridges of fluid between granules of the porous media break. The initial data (2.17) is chosen to be

$$u(x, 0) = 0.9(1 - x^2) + 0.1 \tag{5.2}$$

in the region $x \in [a(t^0), b(t^0)]$, where initially $a(t^0) = -1$ and $b(t^0) = 1$. This initial data is chosen due to its symmetrical nature and also because it adheres to the physically reasonable idea of high to low concentration away from the centre of mass.

5.1.2 Fast Diffusion vs Slow Diffusion

Here, we use the 1D finite element conservation-based moving mesh method described in §4.1 for the PME (2.14) without evaporation to examine the differences between the fast and slow diffusive regimes, for which we take $m = -1.5$ and $m = 1$ respectively. We begin by plotting the initial distribution given in (5.2) for both regimes and advancing the distribution using the same time and space steps for each regime. This will give us an idea of how the distribution develops in each case and also allows us to make quantitative comparisons between the two. We then plot the distribution of the nodal velocities, followed by the development of nodal positions with time to try to develop a clear idea of the differences in the fast and slow diffusive regime models.

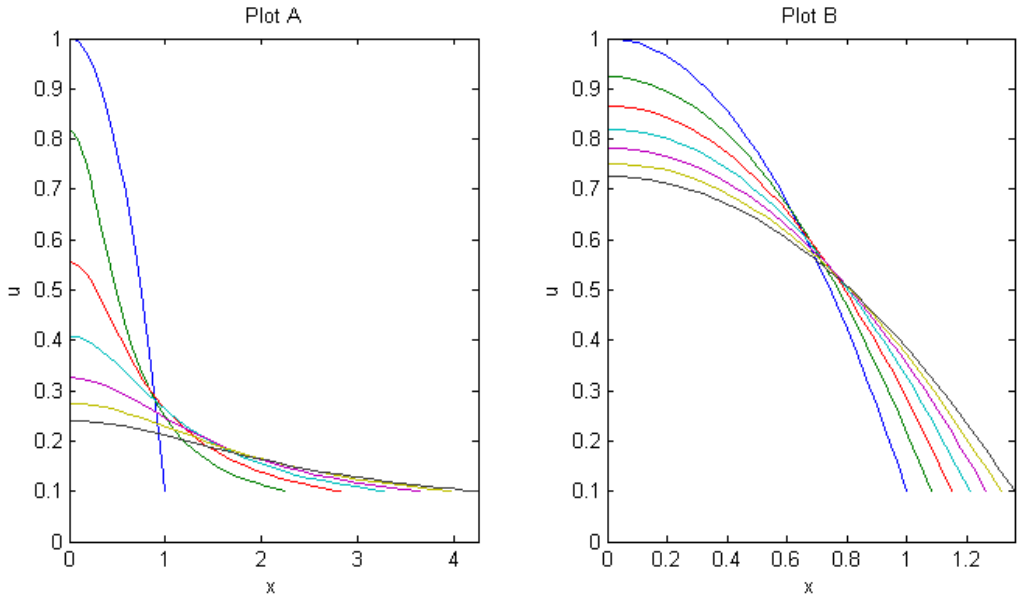

Figure 5.1: Half plane numerical solutions of the PME with Plot A: $m = -1.5$, Plot B: $m = 1$

In figure 5.1 we see that the fast diffusion regime causes a much faster spreading of the distribution of u than the slow regime does. This observation is reflected both in the development of the position of the boundaries and also the rate at which the curve flattens. A further observation is that initially the fast diffusive regime forces a very different distribution to the initial data (although it eventually regains a similar form), whereas the slow diffusive regime keeps much the same shaped distribution as the initial data.

In figure 5.2, showing velocities for the two cases in figure 5.1, we first observe that for both of the fast and slow diffusive regimes the velocity at the origin is zero. This is the case because the initial data (5.2) is symmetric about $x = 0$ which is the centre of mass. (Furthermore, if we were including an evaporation term i.e. for the pme with a source term (2.7) in one dimension, this symmetrical distribution property would remain because the source acts equally on the whole domain.) The plots support some of the ideas developed in the previous paragraph from figure 5.1, since there is approx-

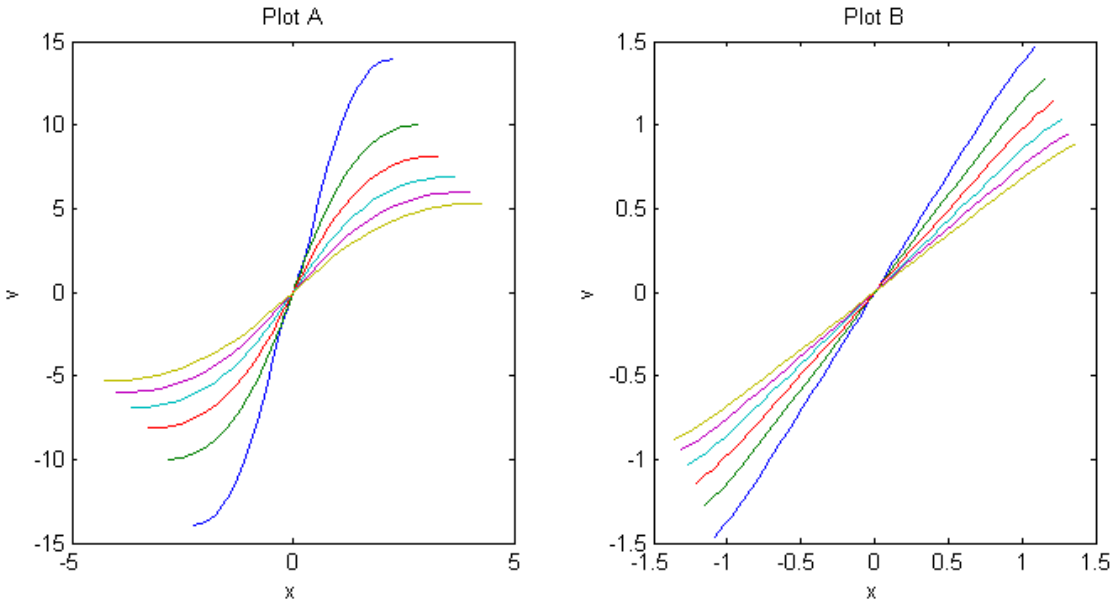

Figure 5.2: Velocities of the nodes for numerical solutions of the PME with Plot A: $m = -1.5$, Plot B: $m = 1$

imately one order of magnitude difference between the velocities of the nodes between the two regimes, explaining how fast the mass spreads for the fast diffusive regime. We also see that for the slow diffusive regime the distribution between the variables is almost linear, which supports the idea of little deformation occuring from the initial spread. For the fast diffusive regime the nodes close to the boundary are moving much faster than those near the origin, displayed by the flattening of the distributions near the boundary positions in Plot A. This supports the idea of larger deformation from the initial data. A further key difference is that the velocities for the fast diffusive regime are decreasing a significant amount more than those for slow diffusion, implying that the fast diffusion process is more powerful initially but tends towards a more similar rate. A final interesting observation for figure 5.2 is that the velocities for fast diffusion keep a similar form throughout the time that the model is run for. This contradicts what was observed in 5.1 where the distribution appeared to initially change from the initial distribution and then return to a similar form.

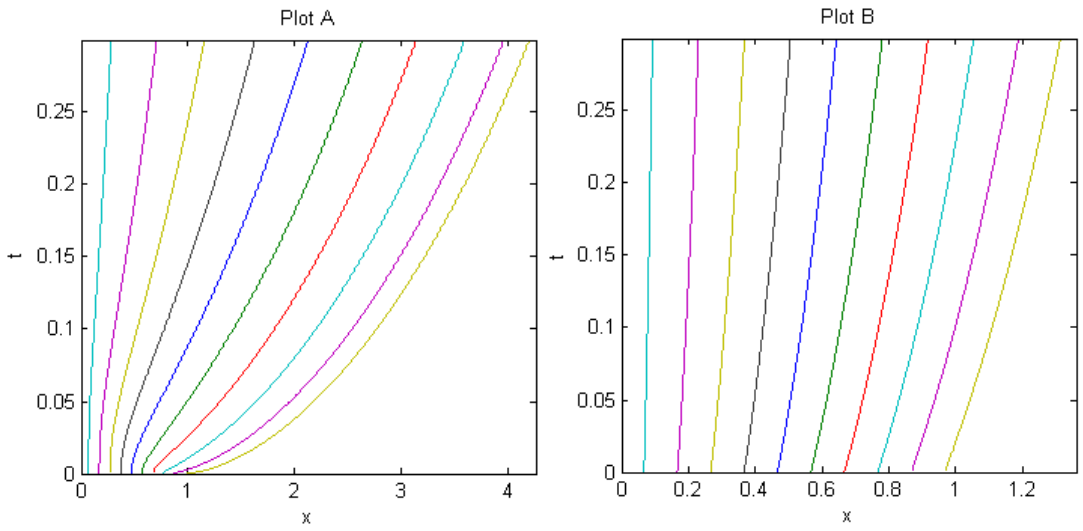

Figure 5.3: Trajectories of the nodes for the numerical solutions of the PME with Plot A: $m = -1.5$, Plot B: $m = 1$

Finially, figure 5.3 shows the trajectories of the nodes from figure 5.1. We see that for the fast diffusive regime, because of the increasing nodal velocities, as we get towards the free moving boundary of u, the distribution initially spreads at a very high rate compared with that of slow diffusion which, as would be expected from Plot B of figure 5.2, stays almost linear. However by the end of the time period Plot A shows that the nodal speed is rapidly decreasing as the gradient appears to tend towards that of Plot B, agreeing with similarities between later distributions in figure 5.1.

The results displayed in this section are all consistent with what we would expect from the PME in the fast diffusion regime, since it contains u^m which becomes large when $m < 0$ and u is small. (We note that the magnitude of m taken, 1.5 for fast diffusion, is not too large as to trigger superfast diffusion [16])

5.1.3 Evaporation effects for fast and slow diffusion

We now take a look at the effects of evaporation on the 2D radially symmetric PME with a source term ((3.37) with $d = 2$) for both the fast and slow diffusive regimes.

(Ideally this would be modelled in 3D, however as mentioned in §3.2.2 this cannot be done in the radially symmetric case since the evaporation only occurs at the boundary which wouldn't be taken into account in the model developed here.)

We plot the elapsed time against the position of the free moving boundary $r(N)$ for both fast and slow diffusion.

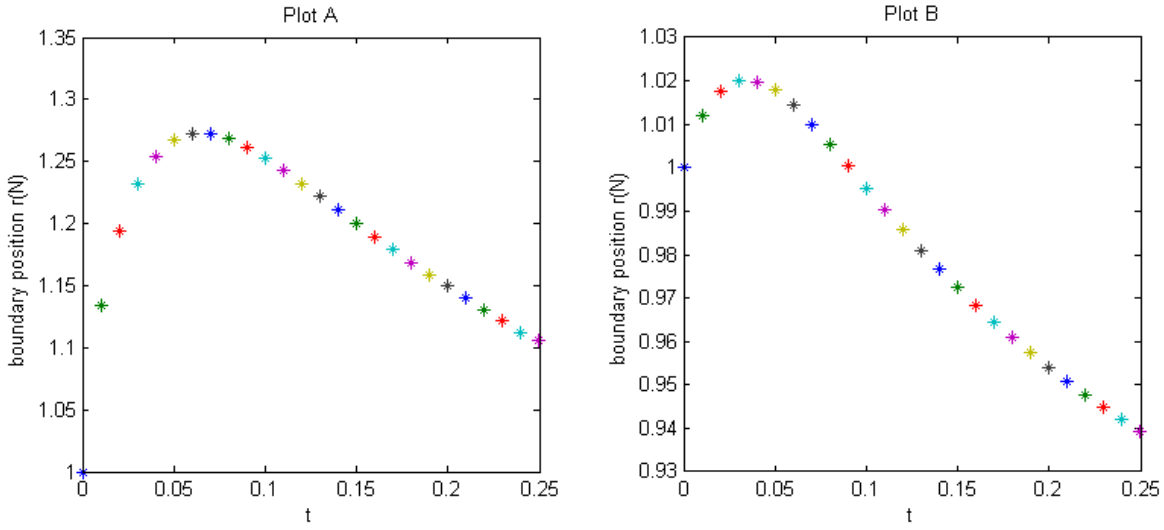

Figure 5.4: Positioning of the free moving boundary $r(N)$ for $s(r) = -5$ for fast diffusion in Plot A ($m = -1.5$) and slow diffusion in Plot B ($m = 1$).

From figure 5.4, which shows the evolution in position of the boundary r_N in time when $s(r) = -5$, we see that under the same conditions (in particular for the same source term), the fast and slow diffusive regimes produce a similarly shaped distribution for the position of the free moving boundary. However Plot A shows that the fast diffusive regime dominates the effect of evaporation for a longer amount of time and has a larger effect on the distance travelled by the free moving boundary than in Plot B. In the time for which this model has been run, the initial effect of fast diffusion is much much stronger than for slow diffusion, forcing the free moving boundary to be advected away more than an order of magnitude further. As well as having a faster rate of diffusion,

the fast diffusive regime also appears to amplify the effect of the source term. After reaching it's peak distance at a later time, the boundary in Plot A recedes around 0.17 spacial units as opposed to around 0.08 spacial units in Plot B.

If we choose the value of $s(r)$ to be too large the distribution of mass falls below the boundary $u = 0.1$ just before the leading edge. This behaviour is unphysical in the context of the prroblem described in §1.1. This is because we chose our boundary conditions and initial data §5.1.1 based on there being a limit at this point, beyond which the liquid capillary network bridges are no longer connected.

5.2 The model problem

We now compare the numerical results to some experimental data. This will give us an idea of how accurately the models work in a particular application. This particular example is representative of those described by the aims set out in §1.1.

The experimental data from the University of Santa Barbara [12] is for liquid spreading of TEHP, which is an organophosphate liquid with low vapour pressure at room temperatures. This means that the evaporation effects will be negligable in this case.

The liquid begins on the surface of the porous medium. Once it has diffused into the medium, only at saturation levels below around 20% can we start to consider the fast diffusion process [12]. We would then expect the geometry to be hemispherical, therefore the most appropriate model we have to compare to experimental data is the one described in §3.1.4 for the radially symmetric PME (3.16) with $d = 3$.

Since the received data has dimensions, we take the PME in the appropriate form, using the derivation in §2.1 and non-dimensionalise it. By doing this we can compare numerical results produced by the program to the non-dimensional experimental results

quantitavely. We begin with the 3D radially symmetric PME in the form

$$\frac{\partial S}{\partial t} = D_0 \frac{1}{r^2} \frac{\partial}{\partial r} \left(\frac{r^2}{(S - S_0)^m} \frac{\partial S}{\partial r} \right) \tag{5.3}$$

where S is the saturation measured as a percentage of full saturation, S_0 is taken to be a fraction of the boundary value and D_0 is the diffusion coefficient with units $m^2 s^{-1}$.

The given data provides the volume in (m^3) of the saturated area, which by the hemispheric geometry gives the position of the boundary, i.e. the radius as

$$R = \left(\frac{3V_0}{2\pi} \right)^{\frac{1}{2}} \tag{5.4}$$

We would like (5.3) in a similar form as (3.16) so we define the non-dimensional variables t' and r' such that

$$r' = \frac{r}{R_0}, \qquad t' = t \frac{D_0}{(R_0)^2} \tag{5.5}$$

where R_0 is a chosen reference boundary position. By substituting these into (5.3) and rearranging we have

$$\frac{\partial S}{\partial t'} = \frac{1}{r'^2} \frac{\partial}{\partial r'} \left(\frac{r'^2}{(S - S_0)^m} \frac{\partial S}{\partial r'} \right) \tag{5.6}$$

This has the Darcy velocity as derived in §3.1.4

$$v = -\frac{\partial S}{\partial r'} \tag{5.7}$$

Using the finite difference algorithm from §3.3.1 we can recover the boundary position r_N. This can then be converted into a volume by the rearrangement of (5.4) allowing a direct comparison to the non-dimensionalised experimental data. For the model we use the intial distribution

$$S^0 = S(b) + (Smax - S(b)) cos \left(\frac{\pi r}{2} \right); \tag{5.8}$$

where S_b is the saturation level at the boundary which is chosen to be the last entry from the values of S in the data. This is an equivalent boundary condition to $u = u_b$ from (2.16), so if the saturation falls below this point then the fluid bridges between

porous grain particles will break and the model no longer applies. The value $Smax$ is the highest level of saturation from the data set. From (5.8), the factor $(Smax - S(b))$ in front of the cosine function is equivalent to k from (2.17). The results are as follows:

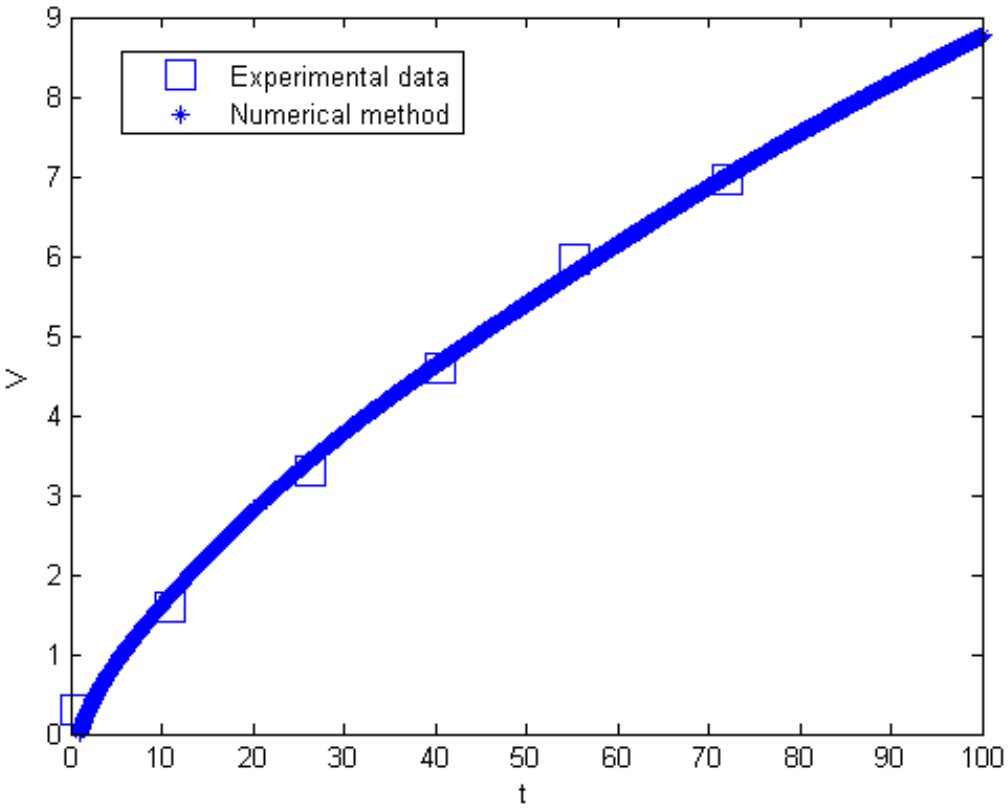

Figure 5.5: Numerical solutions of the radiall symmetric 3D PME plotted against values from experimental data.

From figure 5.5 we see that there is a very good match between the numerical method output and the experimental values. Therefore for this data set we can conclude that the model provides a good representation for fast diffusion in porous media.

Chapter 6

Conclusions and further developments

In this final chapter we summarise the work carried out in this project, followed by ideas for future development in this area of research.

6.1 Summary

In this dissertation we have looked at a variety of ways in which to use a velocity based moving mesh method to model both fast and slow diffusion in a porous medium. In particular, we have implemented such a numerical method in various geometries for the fast diffusion process and found a strong correlation between the output produced and experimental data modelling a chemical agent diffusing in a porous substrate under similar conditions.

We worked throughout the project on a one-dimensional domain. In Chapter 3 we began by formulating a velocity based moving mesh method based on the principle of local mass conservation, in order to model the evolution of the PME in time. This was done in both 1D Cartesian coordinates and also in d-dimensional radially symmetric coordinates. The advantage of the radially symmetric coordinates was that we could

model 3D spherical phenomenon in 1D, making the later comparison with experimental results possible. Using the same coordinate systems we then modelled the PME with a source term to represent evaporation happening within the domain under the principles of conservation of mass fractions.

In Chapter 4 we followed up the work from the previous chapter by deriving a finite element formulation of the problem. This used a similar methodology with a velocity based moving mesh method employed for both the mass conserving and evaporative situations. This was modelled in 1D Cartesian coordinates. Had it not been for time constraints the model would have been moved into higher dimensions. It would have been of particular interest to be able to extend the model to 3D finite elements, since this would have provided the opportunity to model the evaportation process at the boundaries of a 3D domain. The model output could then have been compared to the appropriate experimental data, further developing the framework of applications to be considered.

In Chapter 5 we discussed the results, which were split into two main sections. We began from a mathematical modelling standpoint by using the various models to compare the fast and slow diffusive regimes, followed by comparisons between the effects of incoorporating evaporation into both of these cases.

Finally we looked at results from an experimental point of view. We ran the most appropriate model with some conditions imparted by experimental data from [12] and compared the output of the numerical model to the normalised experimental data. This produced a strong correlation between the model output and the experimental data providing an impetus that the ideas conveyed in this dissertation should be carried further. Since we have only compared the model to one set of results, we cannot draw any concrete conclusions, but it is a good indicator that the methods presented in this dissertation could potentially provide a framework for the effective modelling of

fast diffusion in porous media, in general geometries.

6.2 Future work

To complement this dissertation we now suggest some ideas for future development in this area.

Evaporation

Currently, outside this dissertation there is apparantly no work within this application of how to model evaporation mathematically. Ideally the next development in this field would be to accurately model this process. However this poses several difficulties. Firstly more experimental data would be required for a liquid known to evaporate within a known rate of evaporation. Using this rate of evaporation in the source term for the CPME (2.7) would then hopefully provide a reasonable set of numerical results in comparison to the experimental data. A further problem in modelling fast diffusion with evaporation is that when comparing to experimental results, the model needs to be 3D. However as stated in earlier sections the 3D radially symmetric approach does not do this in the model presented here, because by the nature of the source term it acts on every node. The ideal next step would be to modify a 3D finite element program to include evaporation from the boundary.

Another idea is to use a different type of source term. As an example a time-periodic function could be used to represent a higher rate of evaporation during the day, compared to at night.

A further exploitation of the evaporation process could be to investigate when the saturation falls below a certain threshold and the capillary bridges are no longer connected. Aside from looking at the fate of chemical agents, this could have applications

concerning wet granular systems. Drying and separation of granular molecules can have catastrophic effects such as causing landslides and avalanches.

In the study of the dynamics of wet granular matter knowledge of the levels of saturation within a porous material is highly important. In [11] it is described how dry sand acts as if it were in a liquid state, whereas saturated sand can be formed into reasonably stable structures. A particular example is presented in [11] of a large landslide where a part of the slope has moved downwards and has left a parabola shape in the remaining earth, implying that it was in a viscous liquid state as it fell. A further observation is that the adjacent parts of the land where conditions would most likely be similar nothing has happened. This could imply that this is a threshold process whereby if the saturation of soil falls below a certain level then it reaches a liquid state.

In the study of avalanches, as described in [10], the water saturation of natural snow cover varies. The snow acts as a porous medium and in general water fills up to 20% of the pore volume. When the saturation level is around 7%, we enter the fast diffusion regime. Saturation below this level can be critical as the bridges between pores might break causing the snow granules to part. On a large scale this could cause an avalanche.

Since the two previous examples include much larger height scales and masses than in the chemical agents problem, when formulating a model for these processes we would need to account for gravity. We therefore would have to take a slightly different approach than we have in this dissertation. However, we would essentially still be modelling the cause of landslides and avalanches by the fast diffusion and evaporation processes.

2D and 3D Finite element method

The natural progression in a modelling sense would be to attempt to increase the Catesian coordinate spatial dimensions for the finite element method. We suggest this approach rather than finite differences because, in general for curved boundaries, the finite element method provides a better approximation to the solution. Modelling with $2D$ finite elements was close to being put into practice for this project and would have provided a good addition to the current framework.

If possible 3D finite elements would be implemented to allow comparisons between the model and experiments for the non mass-conserving evaporation case.

Semi-implicit timestepping

For the results we have produced in this dissertation, it has not been necessary to employ the semi-implicit timestepping method derived in §3.1.3. This is due to the low computational demands of the programs. However if we wanted to run the model to produce results over a much longer period of time then the small timesteps needed for the explicit scheme could become an issue, in which case the use of semi-implicit timestepping could become essential.

Furthermore, semi-implicit timestepping can applied to the 1D finite element method, which would have been implemented had it not been for time restrictions.

Self similar solution

Since the main aim of this dissertation was to try to create a model agreeing with physical phenomena it had seemed unnecessary to worry about the analytical properties of the PME. However, to take a more rigorous approach self-similar solutions could be compared to check the accuracy of the numerical methods. The self similar solutions are well documented for the mass conserving slow diffusion process for example see [7]

for the $1D$ cartesian version and see [3] for the $1D$ radially symmetric version. However these would not have been useful in the fast diffusive regime, which is another reason why similarity solutions have not been followed up in this dissertation.

Other meshing techniques

We finally consider two ways in which to adjust the mesh being used.

In order to increase the accuracy of the moving mesh method, the initial mesh can be altered. One way is to create an optimal initial mesh as in [1]. This essentially adjusts the initial distribution of the mesh so as to minimize the L_2 norm of the difference between the approximation to the initial conditions to and the exact initial function over the mesh values.

Another reason to alter the initial mesh is when higher resolution is required in a particular part of the solution. One way in which this can be done is by using equidistribution which relocates grid points without increasing the total number of them. Altering the initial mesh in this way could be useful for example, when tracking a moving boundary by increasing the resolution near the boundary.

Bibliography

[1] M. Baines, *Algorithms for optimal discontinuous piecewise linear and constant l_2 fits to continuous functions with adjustable nodes in one and two dimensions*, Mathematics Of Computation, 62 (1994), pp. 645–669.

[2] M. Baines, M. Hubbard, and P. Jimack, *A moving mesh finite element algorithm for the adaptive solution of time-dependent partial differential equations with moving boundaries*, Appl. Numer. Math., 54 (2005), pp. 450–469.

[3] M. Baines, M. Hubbard, and P.K.Jimack, *Velocity-based moving mesh methods for nonlinear partial differential equations*, Commun. Comput. Phys., 10 (2011), pp. 509–576.

[4] J. Bear, *Dynamics of Fluids in Porous Media*, Dover Publications, 1972.

[5] B. Bhattacharya, *MSc thesis: A moving finite element method for high order nonlinear diffusion problems*, 2006. University of Reading.

[6] K. Blake and M. J. Baines, *Moving mesh methods for nonlinear partial differential equations*, Numerical Analysis Report, Dept of Mathematics, University of Reading, (2001).

[7] C. Budd, G. Collins, W. Huang, and R. Russell, *Self-similar numerical solutions of the porous medium equation using moving mesh methods*, (2008).

[8] C. Budd, W. Huang, and R. Russell, *Adaptivity with moving grids*, Acta Numerica, (2009), pp. 1–131.

[9] W. Cao, W.Z.Huang, and R. Russell, *A moving-mesh method based on the geometric conservation law*, SIAM J. Sci. Comput., 24 (2002), pp. 118–142.

[10] A. Denoth, *Wet snow pendular regime: the amount of water in ring-shaped configurations*, Cold Regions Science and Technology, 30 (1999), pp. 13–18.

[11] S. Herminghaus, *Dynamics of wet granular matter*, Advances in Physics, 54 (2005), pp. 221–261.

[12] A. Lukyanov, *Private communication*, 2011.

[13] K. Morton and D. Mayers, *Numerical Solution of Partial Differential Equations*, Cambridge University Press, 1994.

[14] K. Osman, *MSc thesis: Numerical schemes for a non-linear diffusion problem, msc dissertation*, 2005. University of Reading.

[15] J. Parker, *MSc thesis: An invariant approach to moving-mesh methods for partial differential equations*, 2010. University of Oxford.

[16] M. Peletier and H. Zhang, *Self-similar solutions of a fast diffusion equation that do not conserve mass*, (1994).

[17] J. Vazquez, *The Porous Medium Equation*, Oxford Science Publications, 2007.

[18] P. Wesseling, *Computational Fluid Dynamics*, Springer, 2000.